Cross Diabolo Hollow Notch Nanotweezer for Optical Trapping and Manipulation

Md. Abeed Hasan and Ahmed Zubair, *Senior Member, IEEE*

***Abstract*—Plasmonic nanotweezer manipulates nanoparticles utilizing extraordinary electric field gradients and field enhancement originated from localized surface plasmon resonance. We proposed an ingenious silver-based cross diabolo hollow notch plasmonic nanotweezer. Additional edges at the center maximize the field enhancement caused by local surface plasmon hot spots. Moreover, the bottom Ag film's screening effect significantly increases the field intensity near the trapping targets. The subsequent field gradient remarkably enhances the trapping capability of the design in comparison to conventional plasmonic tweezers. We carried out a comprehensive analysis of structural design optimization to reduce power consumption and significantly improve optical trapping properties. The proposed Ag CDHN nanotweezer can trap a polystyrene sphere of 30 nm diameter at a minimum beam intensity of 2.66 mW/μm^2 and trapping force of 2.14 nN/(W.μ m^{-2}) towards the nanostructure. In comparison to previously reported nanotweezers, the proposed nanotweezer demonstrated a few-order increase in trapping stiffness and a few times decrease in power consumption. We also evaluated its capacity to trap polystyrene spheres of varying diameters. Our proposed design and analysis will be beneficial in realizing effective nanotweezer for nanoparticle manipulation as well as nanostructure fabrication.**

***Index Terms*—Nanotweezer, optical trapping, plasmonics, optical force, cross diabolo hollow notch.**

I. Introduction

IN OPTICAL tweezers, the field gradient due to a highly focused laser beam exerts trapping force toward the focus of the beam on minuscule particles. This distant-controlled and non-destructive technique has paved various applications for the manipulation and characterization of dielectric nanoparticles [1]–[5] and living cells [6]–[8]. However, stable trapping of particles smaller than the incident beam wavelength is difficult due to the blunt gradient field observed by the particle. Plasmonic metallic nanostructures can be utilized for developing sufficient field gradients using low-powered sources. These structures can create localized surface plasmon resonance (LSPR) where free charges accumulate at different edges of the metal-dielectric interface for selective incident wavelengths, known as resonance wavelengths [9]. Metallic structures equipped with nano-gap can accumulate charges precisely at the edges of the nano-gap at one of its resonance wavelengths [10]. It amplifies the electromagnetic (EM) field at the metal edges near the gap location which is generally referred to as 'hot spots'. Some metallic structures can further amplify the hot spot field enhancement process when the lightning rod effect occurs due to structural edges of metal [11]. These hot spots originate magnified EM field over source field. Hence, generated sharp field gradient makes trapping of sub-wavelength sized particles feasible. Typically Ag and Au are the preferred metals for plasmonic tweezers due to their low plasmonic loss and superior field enhancement capability [12], [13]. There are several reports of developing hot spots in nanostructures such as nanodiscs [14], nanoholes [1], [15], and bowties [16]–[18]. However, such plasmonic nanotweezers exhibit Joule heating due to the strong absorption losses [19]. This generally elevates the temperature around the hot spots and the resultant temperature gradient can cause thermophoresis and convection. Alternatively, dielectric waveguide-based nanotweezers can mitigate this issue. A variety of dielectric nanostructures capable of producing narrow field gradients have been reported such as nanoantenna [20]–[22], artificial photonic lattices [23], [24] and cavity [15], [25]. However, they require a larger footprint to maintain resonant modes and also require a comparatively high-powered source over plasmonic ones. Research has been conducted to mitigate heating issues related to plasmonic tweezers. Wang *et al.* utilized metal with a high thermal conductivity as heat sink film and placed it below the plasmonic nanostructure to dissipate heat quickly from the hot spots [26].

Bowtie is one of the efficient geometries among basic plasmonic nanotweezers. Several bowtie-inspired structures were reported exceeding performance over the conventional one [9], [13], [27]–[31]. Hrtoň *et al.* studied EM characteristics of bowtie, diabolo (bridged bowtie) and both their aperture structures [32]. According to this report, diabolo aperture contributed dominant field enhancement due to the combination of lightning rod and nano-gap effect. Besides, Gupta and Dhawan reported that cross diabolo aperture (CDA) can furnish superior field enhancement compared to diabolo aperture because of the increased number of hot spots [9]. Lin and Lee worked on Au-based mono DHN by adding an Au film at the bottom of Au diabolo aperture [33]. The additional metal film reflected the light energy which used to get wasted due to propagating through the transparent gap region in metal film-less structures. This reflection of energy shifted major charge accumulation at the top edges of the nanotweezer. Thus, effective field enhancement

Manuscript received February 6, 2022; revised March 8, 2022; accepted March 10, 2022. Date of publication March 25, 2022; date of current version March 31, 2022. *(Corresponding author: Ahmed Zubair.)*

The authors are with the Department of Electrical and Electronic Engineering, Bangladesh University of Engineering and Technology, Dhaka 1205, Bangladesh (e-mail: abeedhasan22@gmail.com; ahmedzubair@eee.buet.ac.bd).

This article has supplementary downloadable material available at https://doi.org/10.1109/JPHOT.2022.3159735, provided by the authors.

Digital Object Identifier 10.1109/JPHOT.2022.3159735

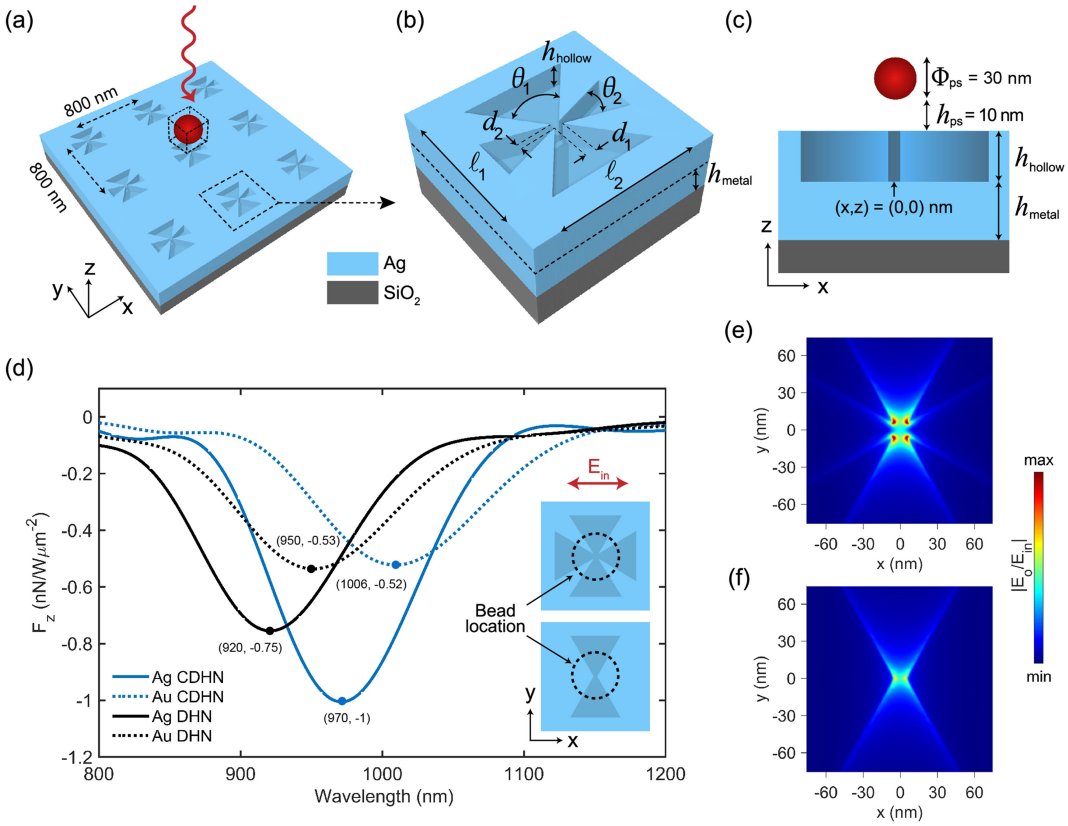

Fig. 1. Schematic representations of (a) 3x3 arrays and (b) truncated unit-cells of proposed CDHN nanotweezers. (c) Visual representation of a PS bead of 30 nm diameter placed at center of the xy-plane above the nanotweezer where $h_{ps} = 10$ nm. (d) Wavelength dependence of F_z for CDHN (blue line) and DHN (black line) nanotweezers where dotted and solid lines represented Au and Ag as selected metals, respectively. E-field intensity on xy plane at the top metal surface of (e) Ag CDHN at $\lambda_d = 970$ nm and (f) Ag DHN at $\lambda_d = 920$ nm.

positively impacted particle trapping. Moreover, Ag can provide marginally improved reflectivity at IR regime and thermal conductivity over Au which left an option to further elevate the trapping performance.

In this work, we proposed an Ag cross diabolo hollow notch (CDHN) nanotweezer by adding Ag film at the bottom of CDA. Ag CDHN can be a more efficient and cost-effective bowtie-inspired plasmonic nanotweezer design combining the benefits of CDA and bottom metal film. We theoretically analyzed the underlying physics behind the shifting of suitable trapping beam wavelength and consequent trapping performance for varying design parameters. Ag DHN nanotweezer, which we found as a very efficient tweezer design over conventional diabolo ones in our previous study [34], is outperformed by our current proposed Ag CDHN nanotweezer. For different diameters of polystyrene spherical (PS) beads, change of trapping force components and shifting of the trapping beam wavelength were also investigated which will be beneficial to implement this kind of nanotweezer for particle detection applications.

II. Structural Design and Simulation Setup

A. Structural Design

Our CDHN structure is composed of metal-based CDA structure on top of an analogous metal thin film. The metal structure is supported on a glass (SiO_2) substrate. The illustrations of the 3x3 array and unit cell of the CDHN nanotweezer are presented in Figs. 1(a) and Figs. 1(b), respectively. For suspended particle trapping, the whole system was considered to be immersed in water ($n_{water} = 1.33$). Heights of structural aperture and thin metal film were denoted by h_{hollow} and h_{metal}, respectively. In the CDHN structure, both diabolo hollow notches were perpendicular to each other and a common gap was created at the center. The central gap region of CDHN was termed as horizontal gap length, d_1 and vertical gap length, d_2. Wing lengths of vertical and horizontal diabolo notches were l_1 and l_2, respectfully. Hollowed bow angles of vertical and horizontal diabolo notches were θ_1 and θ_2, respectfully. The periodicity of each cell of CDHN nano-array was considered to be 800 nm in x and y directions. Fabrication process of the proposed nanostructure is provided in Supplementary Material.

B. Methodology

Finite difference time domain (FDTD) solver was used for analyzing properties of the proposed plasmonic nanotweezer. FDTD method provides faster convergence and better accuracy for these kind of structures compared to other methods. Perfectly matched layer (PML) boundary conditions were used in all directions during simulation. Complex dielectric constants of both Ag and Au were adopted from Johnson and Christy [35]. Material properties of glass were acquired from Palik [36]. Finite

element solver was utilized for heat transfer analysis. Thermal properties of Ag was adopted from CRC [37].

In order to mimic viruses or proteins or dielectric nanoparticles, a nanoscale PS bead of diameter, $\Phi_{ps} = 30$ nm was chosen as a trapped particle. The refractive index of PS bead, n_{ps} was 1.57. For trapping force calculation, PS was surrounded by six 2D field monitors. The resultant EM fields were post-processed into 3D optical force using the time-averaged closed surface integral of Maxwell stress tensor as shown in (1) [38].

$$\boldsymbol{F} = \oint_s (\boldsymbol{T}.\,\boldsymbol{n})\,\mathrm{d}s, \tag{1}$$

where $\boldsymbol{F}$ is time-averaged force, $\boldsymbol{n}$ is unit vector perpendicular to the integration surface and $\boldsymbol{T}$ is time-averaged Maxwell stress tensor which can be presented as,

$$\boldsymbol{T} = \frac{1}{2}\mathrm{Re}\left[\varepsilon \boldsymbol{E}\boldsymbol{E}^* + \mu \boldsymbol{H}\boldsymbol{H}^* - \frac{1}{2}(\varepsilon \boldsymbol{E}^2 + \mu \boldsymbol{H}^2)I\right], \tag{2}$$

where $\boldsymbol{E}\boldsymbol{E}^*$ and $\boldsymbol{H}\boldsymbol{H}^*$ denote outer products of electric field ($\boldsymbol{E}$) and magnetic field ($\boldsymbol{H}$), respectively. $\boldsymbol{I}$ is the identity matrix and ε, μ are the permittivity and the permeability of the medium, respectively. Detailed equations for force components are provided in Supplementary Material. The trapping potential along x axis was obtained by $\int F_x\,\mathrm{d}x$, where F_x is the x component of optical force. Similarly, trapping potential along y and z axes were calculated.

During simulation, the backscattering spectrum only provides information about LSPR wavelength while being unspecific about the location of the hot spot. At certain resonance wavelengths, LSPR mode can occur at side edges rather than the edges near the central gap which will not enhance trapping performance. Therefore, structural optimization using backscattering spectrum is defective. Typically, E-field intensity is monitored at the edges near the central gap to detect LSPR wavelength. Nevertheless, effective trapping of any nano-particle requires contributions from both electric and magnetic fields, shown in (2). Therefore, neglecting magnetic field data may deviate from accurate outcomes. For more meticulous approximation, a PS bead can be placed above the plasmonic nanotweezer at the horizontal center of the structure to observe the wavelength dependence on optical force along z direction, F_z. The spectrum of F_z has notches or dips when field enhancement peaks at the central metal gap. In our analyses, we only focused on the lowest dip of F_z when particle can be trapped effectively at that corresponding wavelength. For future discussions, the lowest dip of F_z and the corresponding trapping beam wavelength are denoted by F_d and λ_d, respectively.

III. Characteristic Study of Proposed Structure

A. Mono and Cross Diabolo Hollow Notch

Trapping performance of DHN and CDHN was evaluated for Au and Ag as the metals. For CDHN nanotweezer, selected parameters were $l_1 = l_2 = 300$ nm, $\theta_1 = \theta_2 = 60°$, $d_1 = d_2 = 10$ nm and $h_{hollow} = h_{metal} = 70$ nm. For DHN nanotweezer, only vertical diabolo of CDHN was considered with identical parameters i.e., $l_1 = 300$ nm, $\theta_1 = 60°$, $d_1 = 10$ nm and $h_{hollow} = h_{metal} = 70$ nm. A PS bead of 30 nm diameter was placed at center of the xy-plane above the nanotweezer where $h_{ps} = 10$ nm (see Fig. 1(c)). The incident beam was x-polarized plane wave.

For a conscientious selection of geometry and material for the nanostructure, spectra of F_z for both structures based on Au and Ag is displayed in Fig. 1(d). Moreover, E-field intensity distribution on the top surface of metal layer for Ag based DHN and CDHN nanotweezers at corresponding λ_d are presented in Figs. 1(e) and Figs. 1(f), respectively. When both structures were compared to associated metals, Au-built structures had a higher λ_d than Ag-built structures. Ag-based structures had a better screening effect which contributed to more E-field intensification at the top metal surface. Hence, nanotweezers made of Ag had a higher $|F_d|$ than those made of Au. Furthermore, Ag provides heat sink capability comparable, if not better, than that of Au. CDHN had four hot spots on the top metal interface, whereas DHN had only two. As a result of the increased surface plasmon coupling, a redshift in λ_d was observed for CDHN compared to DHN, which is consistent with a previous report [9]. As fabrication of CDHN is more detailed than DHN, using Au to achieve similar performance (see dotted lines of Fig. 1(d)) is not recommended. As a result, mono diabolo or bowtie-type structures are better suited to be fabricated using Au [10], [39]. However, Ag CDHN could provide up to 33% more $|F_d|$ than Ag DHN due to increased charge accumulation at the center for CDHN's narrow bow angles. For the reasons stated above, Ag is chosen for the proposed CDHN nanotweezer.

B. Bottom Metal Film Induced Plasmon Coupling and Screening Effect

The color map of $|F_z|$ spectra for Ag CDHN nanotweezer by sweeping h_{metal} from 0 to 150 nm is presented in Fig. 2(a). Other parameters were unchanged during the simulations. Fig. 2(b) presents zoomed spectra of $|F_z|$ for sweeping h_{metal} from 0 to 6 nm for better visualization of the resonance peak in the longer wavelengths. The increase of h_{metal} blueshifted λ_d from 1960 nm until it saturated at 970 nm when h_{metal} exceeded 35 nm. Fig. 2(d)–(f) show E-field intensity on xz-plane along y axis for $h_{metal} = 0$ nm, 5 nm and 50 nm, respectively at corresponding λ_d. When $h_{metal} = 0$ nm, the structure transmutes into CDA structure on a glass substrate. Free charge accumulation resulted in E-field enhancement at top and bottom edges of metal surface which is consistent with the previous reports [30], [40]. Charge density at the central metal edges which were distributed along the vertical surface, accommodated strong surface plasmon coupling resulting in λ_d at 1960 nm as can be seen in Fig. 2(d) [41]. Charge localization near the bottom edges of metal surface fell rapidly for minimal addition of Ag metal film ($h_{metal} = 5$ nm) at the bottom, presented in Fig. 2(e). Due to disruption in surface plasmon coupling, blueshift of λ_d was observed for increasing h_{metal} up to 35 nm. After h_{metal} exceeded 35 nm, charges only localized near top edges of metal surface and plasmon coupling factor with the bottom edges became insignificant which is illustrated in Fig. 2(f) where h_{metal} was 50 nm. Therefore, λ_d saturated at 970 nm.

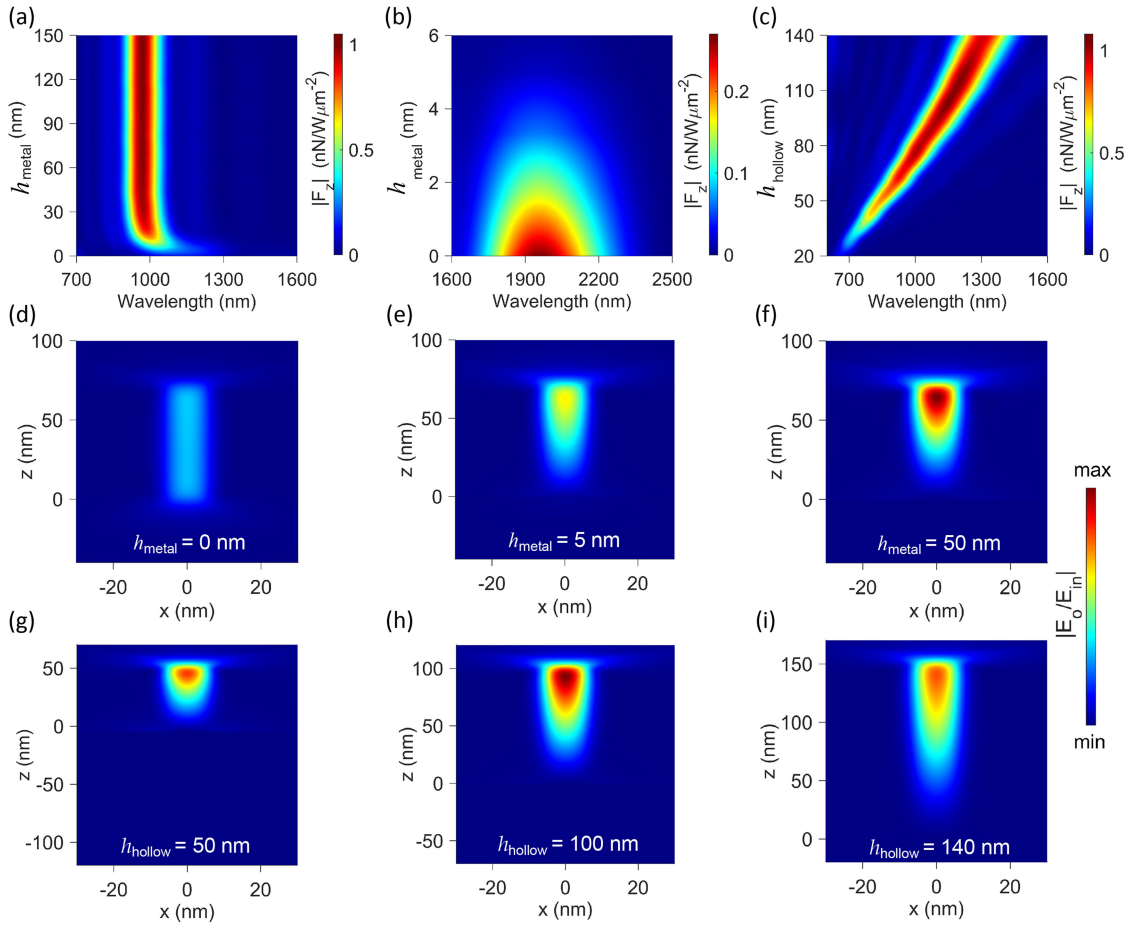

Fig. 2. Color map showing the spectra of $|F_z|$ for (a) varying h_{metal} from 0 to 150 nm where wavelength was ranged from 700 to 1600 nm and (b) varying h_{metal} from 0 to 6 nm with wavelength variation from 1600 to 2500 nm. For both cases $l_1 = l_2 = 300$ nm, $\theta_1 = \theta_2 = 60°$, $d_1 = d_2 = 10$ nm, $h_{hollow} = 70$ nm. (c) Color map illustrating wavelength dependence of $|F_z|$ where h_{hollow} was varied from 20 to 140 nm, $h_{metal} = 150$ nm and other parameters were same as previously stated. E-field intensity on xz-plane along y axis for $h_{metal} =$ (d) 0, (e) 5, and (f) 50 nm at λ_d equal to 1920, 1300, and 970 nm, respectively. Video 1.mp4 depicts a movie illustrating the change in E-field intensity as h_{metal} was swept from 0 to 130 nm at the corresponding λ_d. E-field intensity on xz-plane along y axis for $h_{hollow} =$ (g) 50, (h) 100, and (i) 140 nm at corresponding $\lambda_d = 850$, 1125, and 1300 nm, respectively. Video 2.mp4 demonstrates a movie showing the variation of E-field intensity for ranging h_{hollow} from 20 to 140 nm at corresponding λ_d.

For increasing h_{metal}, $|F_d|$ incremented from 0.4 $\mathrm{nN/W}\mu\mathrm{m}^{-2}$ until it saturated at 1 $\mathrm{nN/W}\mu\mathrm{m}^{-2}$ when h_{metal} exceeded 35 nm. Light reflects energy towards the upper metal edges due to screening effect when bottom metal film is present. Both screening effect and lightning rod effect accumulate more charges at the top corners and enhance E-field intensity at the top surface where a PS bead is placed and similar behavior was reported before [33]. Thus, increment in $|F_d|$ was observed for increase in h_{metal} up to 35 nm. Due to saturation of screening effect, $|F_d|$ saturated for $h_{metal} \geq 35$ nm.

To observe heat sink capability of the proposed structure, 0.8 mW heat source was introduced at the center of the top surface and h_{metal} was varied from 40 to 150 nm. The resultant temperature profiles along y axis at xz plane can be seen in Fig. 3. Heat conduction and heat sinking capability enhanced for increasing h_{metal}. Therefore, h_{metal} height was selected to be 150 nm which can minimize thermophoresis and convection and will be beneficial for thermally-sensitive nanoparticle manipulation.

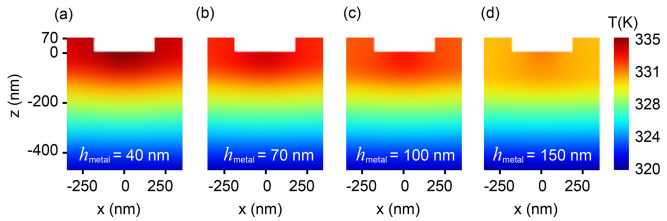

Fig. 3. Temperature profile using 0.8 mW heat source situated at the center for Ag CDHN nanotweezer with $h_{metal} =$ (a) 40, (b) 70, (c) 100, and (d) 150 nm.

C. Effect of Metal Hollow Height

Color map depicting the spectra of $|F_z|$ is presented in Fig. 2(c) where h_{hollow} was varied from 20 nm to 140 nm and other design parameters were set as previously mentioned. λ_d was independent of plasmon coupling between top and bottom metal edges since bottom metal-film height was above the saturation height as demonstrated in Fig. 2(g)–(i), depicting

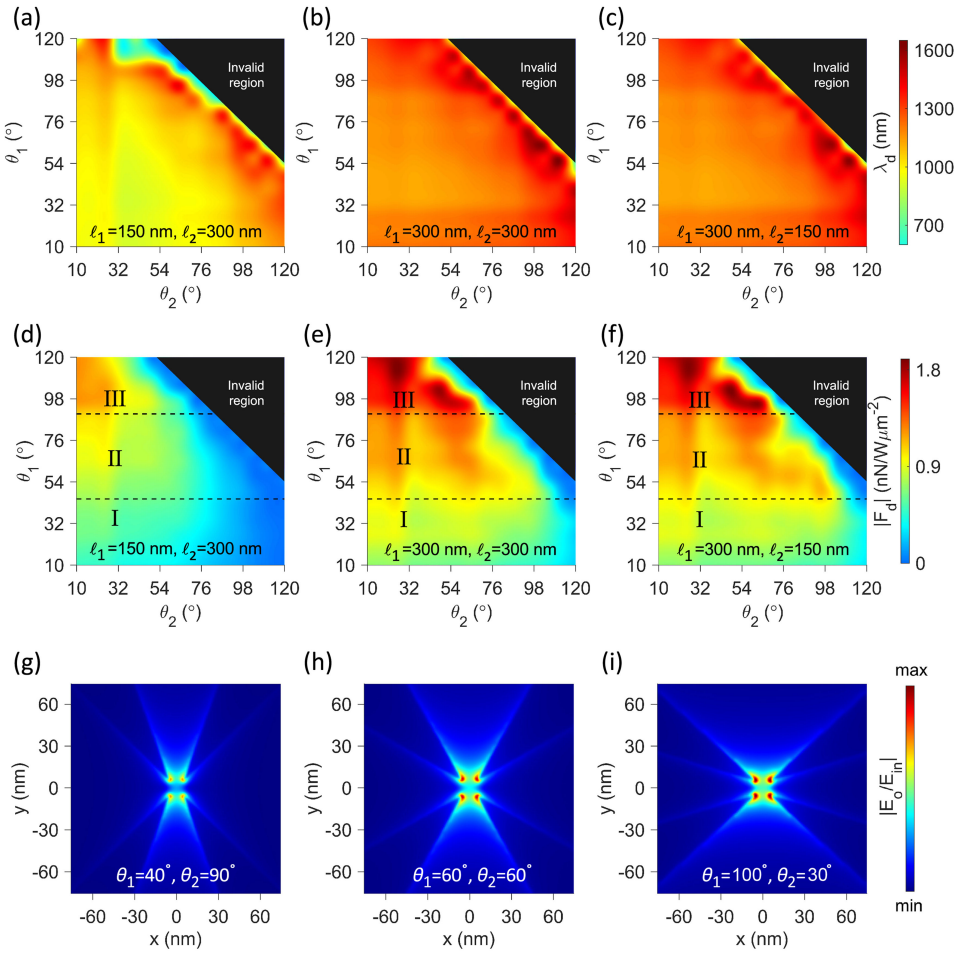

Fig. 4. Color maps showing (a-c) λ_d and (d-f) $|F_d|$ for varying both θ_1 and θ_2 from 10° to 120°. Here, $(l_1, l_2) = (150, 300)$ nm at (a,d), (300, 300) nm at (b,e) and (300, 150) nm at (c,f). Other parameters included $d_1 = d_2 = 10$ nm, $h_{metal} = 150$ nm and $h_{hollow} = 110$ nm. E-field intensity on xy plane at top metal surface of Ag CDHN for $(\theta_1 \ \theta_2) = (40°, 90°)$ at (g), (60°, 60°) at (h) and (100°, 30°) at (i). Corresponding λ_d are 1230, 1200, and 1250 nm.

E-field intensity on xz-plane along y axis for $h_{hollow} = 50$ nm, 100 nm and 140 nm at corresponding λ_d. For increasing h_{hollow}, λ_d redshifted due to larger penetration depth of surface plasmon polariton (SPP) at longer wavelengths [42]. It was experimentally proven that E-field intensity could increase at top metal edge with the decrease of nano-aperture height, which is denoted by h_{hollow} in our design [43]. However, shorter h_{hollow} induced low concentration of charge which lead to lower E-field intensity at the top (see Fig. 2(g)). On the contrary, increasing h_{hollow} instigated charge loss at the upper edges due to charge redistribution along the vertical sidewalls of metal. This resulted in E-field intensity reduction at the top edges shown in Fig. 2(i). Therefore, $|F_z|$ reached a peak value when h_{hollow} was between 80 to 130 nm, according to Fig. 2(c). For further analyses, h_{hollow} was considered to be 110 nm.

D. Plasmon Coupling and Light Polarization-Dependence Due to Bow Angles

Optical trapping properties of the proposed structure depending on both vertical and horizontal hollowed bow angles (θ_1 and θ_2 respectively) were investigated to obtain the optimal design. Figs. 4(a)–(c) and 4(d)–(e) depict color maps of λ_d and $|F_d|$ respectively by sweeping θ_1 and θ_2 from 10° to 120°. To understand the effect of wing lengths on bow angles, $|F_d|$ and λ_d were calculated for 3 different combinations of l_1 and l_2 i.e. (150, 300), (300, 300) and (300, 150) nm. Other structural parameters were kept unaltered. The black regions in the figures represented invalid structure because $\theta_1 + \theta_2 \geq 180°$. Transitions of $|F_d|$ and λ_d remained almost independent of l_1 and l_2 for combinations where $l_1 \geq l_2$. From Fig. 4(b), (c), it is apparent that λ_d redshifted for θ_1 or θ_2 above 90° owing to the increase in effective index of local surface plasmon polaritons (SPPs) [44]. Additional redshift can occur at these cases because of enhanced plasmon coupling at sidewalls adjacent to θ_1 and θ_2 as seen in Fig. 4(g)–(i), illustrating E-field intensity on xy plane at top metal surface of Ag CDHN for $(\theta_1, \theta_2) = (40°, 90°)$, (60°, 60°) and (100°, 30°), respectively at corresponding λ_d (where $l_1 = 300$ nm, $l_2 = 300$ nm). According to these figures, sidewalls adjacent to θ_1 have significant charge accumulation compared to those of θ_2. Therefore, θ_2 above 90° produces marginally larger red-shift over θ_1 above 90°. However, drastic drop in λ_d was observed for the case of $(l_1, l_2) = (150, 300)$ nm (see Fig. 4(a)) due to reduced charge coupling for lower value of l_1.

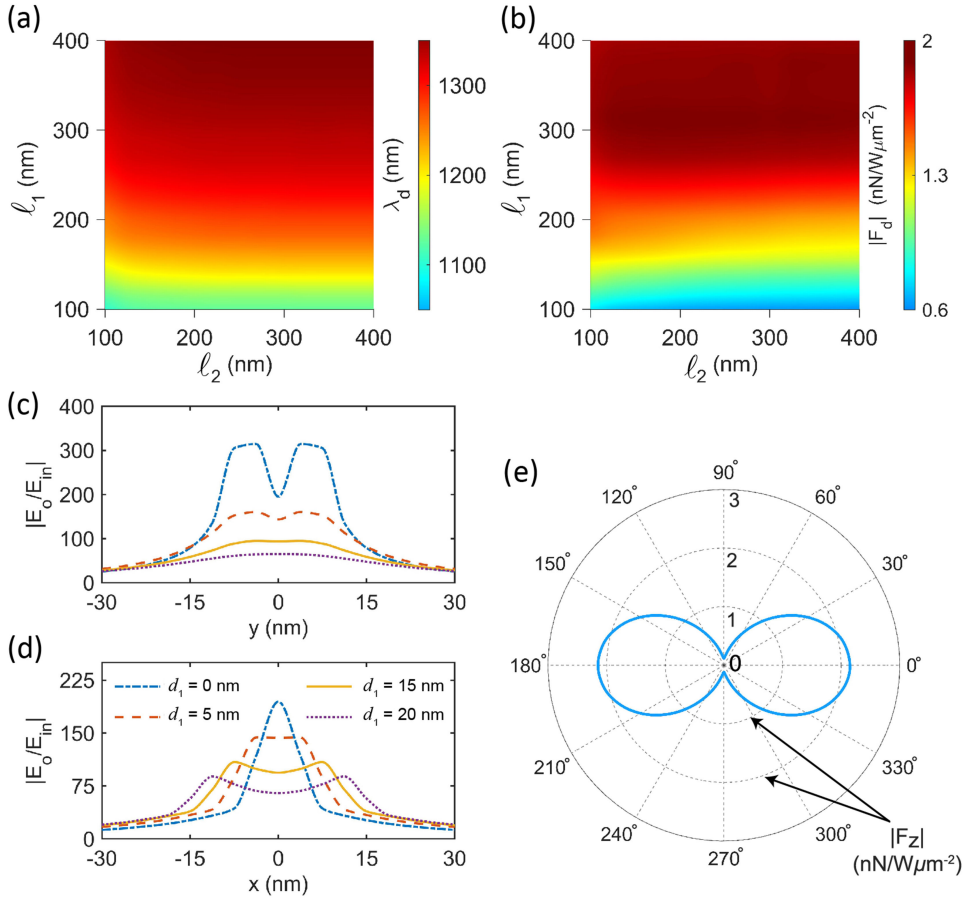

Fig. 5. Color map representations of (a) $|F_d|$ and (b) λ_d where l_1 and l_2 were swept from 100 to 400 nm. Here, $\theta_1 = 115°$, $\theta_2 = 25°$, $d_1 = d_2 = 10$ nm, h_{metal} = 150 nm and h_{hollow} = 110 nm. E-field intensity (c) along y axis and (d) along x axis for $d_2 = 8$ nm and $d_1 = 0$, 5, 15, 20 nm. Here, $l_1 = 315$ nm and $l_2 =$ 200 nm and other parameters were unchanged as before. (e) Polar plot for $|F_z|$ depending on incident beam polarization for the optimized Ag CDHN nanotweezer at 1340 nm incident wavelength. E-field intensity variation with beam polarization is illustrated in Video 3.mp4.

E-field enhancement of the nanotweezer can be explained by dividing Fig. 4(d)–(f) into 3 regions. For increasing horizontal bow angle θ_2, peak E-field at the center dropped for all cases due to the increased perpendicular relation with x-polarized source beam which was consistent with previous reports [17], [45]. When θ_1 was around 10° to 45° (Region I), sidewalls adjacent to θ_1 were perpendicular to the light polarization. Hence, low E-field intensity occurred at the center as can be seen in Fig. 4(g). When θ_1 was around 45° to 90° (Region II), sidewalls adjacent to θ_1 were less perpendicular to light polarization compared to the structures for Region I. Consequently higher E-field intensity was observed as shown in Fig. 4(h). While θ_1 was above 90° (Region III), sidewalls adjacent to θ_1 were almost parallel to light polarization and generate maximum E-filed intensity as shown in Fig. 4(i). Thus, maximum $|F_d|$ could be observed in this region. To avoid complexity during fabrication process, we considered $(\theta_1, \theta_2) = (115°, 25°)$.

E. Redistribution of Accumulated Charge With Variation in Vertical Wing Length

Optical trapping characteristics of the proposed structure were monitored by varying vertical wing length, l_1 and horizontal wing length, l_2. Fig. 5(a) and (b) represent colour maps of λ_d and $|F_d|$ respectively for varying l_1 and l_2 from 100 to 400 nm while setting other parameters as mentioned before. Increasing l_1 engaged more charge coupling at the sidewalls adjacent to θ_1 (see Fig. S3 of Supplementary Material). Thus, red-shift was observed for increasing l_1. However, resonance wavelength remained mostly unaltered for the increment of l_2 due to less dominance of charge localization at the sidewalls adjacent to θ_2. Consequently, $|F_d|$ was also mostly independent of l_2. Screening effect provided less impact for lower values of l_1 [33]. Thus, decline in $|F_d|$ was noticed for l_1 decreasing from 250 to 100 nm. Moreover, charges redistributed more along the sidewalls while dropping at the central edges for increased values of l_1. Therefore, $|F_d|$ started to drop for l_1 over 330 nm. Both these effects were minimized when l_1 was ranging from 250 to 330 nm. According to simulation results, maximum $|F_d|$ was detected at $l_1 = 315$ nm and $l_2 = 200$ nm which were considered for further analyses.

F. Charge Coupling and Overlapping Factor for Gap Distance

λ_d and $|F_d|$ were calculated by varying horizontal gap, d_1 and vertical gap, d_2 from 0 to 20 nm as can be seen in the

color maps of Fig. S4 in Supplementary Material. Increment of d_1 resulted in reduced charge coupling between adjacent corners related to θ_1 where major charge accumulation occurred. Hence, λ_d blueshifted. Increment of d_2 had insignificant impact on λ_d because of low charge accumulation from adjacent sidewalls related to θ_2.

However, $|F_d|$ had inconsistent dependence on d_1 and d_2. It can be explained by combining effects of target-field overlapping factor and E-field intensity applied over the PS bead. For better understanding, E-field intensity was observed along y axis (see Fig. 5(c)) and along x axis (see Fig. 5(d)) for $d_2 = 8$ nm and $d_1 = 0$, 5, 15, 20 nm. Peak E-field intensity along x and y axis attenuated more with the increase of d_1. Simultaneously, peak E-field shift followed central edges creating dual modes and increased E-field spreading which lead to amplified target-field overlapping factor. Combined contribution of target-field overlapping factor and E-field intensity over a 30 nm diameter PS bead resulted in maximum $|F_d|$ for (d_1, d_2) = (5, 8) nm which was considered for further analyses.

G. Polarization Sensitive Optical Trapping

Spectra of EM-field at the central location is illustrated at Fig. S5 in Supplementary Material. According to these analyses, the required incident wavelength for efficient trapping was 1340 nm. Incident beam polarization dependence on $|F_z|$ of the optimized Ag CDHN is illustrated at the polar plot in Fig. 5(e). The nanotweezer exerted maximum $|F_z|$ for x polarized incident beam as the design was optimized considering this condition. $|F_z|$ dropped due to low charge accumulation at the central edges when incident light polarization was rotated towards y axis.

IV. Analysis on Nanoparticle Trapping

Trapping forces and potentials were investigated considering x-polarized plane wave illumination for a unit cell of nanotweezer. Due to structural symmetry, only certain force components were required to visualize the trapping incident. Therefore, F_x, F_y and F_z were calculated for a PS bead moving along x, y and z axis, respectively. When the bead was moved along x and y axis, it was considered to be positioned at $h_{ps} =$ 10 nm along z axis. Corresponding potentials (U_x, U_y, U_z) were normalized in $k_B\mathrm{T}/\mathrm{W}\mu\mathrm{m}^{-2}$ unit, where k_B is the Boltzmann constant and T is the ambient temperature (300 K). Vital trapping force components and corresponding potentials of optimized Ag CDHN and Ag DHN are displayed in Fig. 6(a)–(c) for $\Phi_{ps} =$ 30 nm. Both nanotweezers had lower F_x compared to F_y because of reduced resultant E-field contribution. Thus, a small potential depth was observed in U_x compared to U_y in both nanotweezers. While comparing both nanotweezers, proposed CDHN have 100%, 43% and 84.2% improved peak to peak trapping forces (of F_x, F_y, F_z respectively) over DHN. Furthermore, potential wells of U_x, U_y and U_z raised by 83.5%, 20% and 122%, respectively. Hence, a significant improvement of optical trapping can be achieved using Ag CDHN. Moreover, the proposed CDHN nanotweezer will require a low-powered light source to achieve identical trapping performance. For stable trapping, the requirement of minimum potential depth is $-10\ \mathrm{k_B T}$. The proposed nanotweezer can trap a PS bead of 30 nm diameter at x = y = 0 for illumination intensity above 2.66 $\mathrm{mW}/\mu\mathrm{m}^2$ while DHN will require intensity above 4.85 $\mathrm{mW}/\mu\mathrm{m}^2$. Additionally, inward force of 2.14 nN/(W.$\mu\mathrm{m}^{-2}$) and 1.14 nN/(W.$\mu\mathrm{m}^{-2}$) was observed for the above cases, respectively. The proposed nanotweezer provided enhanced trapping stiffness (k_x, k_z) over DHN nanotweezer as can be seen in Table I. Stiffness parameters were approximated considering tangential forces at $(x, y, z) =$ (0, 0, 110) nm.

TABLE I
The Trapping Stiffness Along Different Direction

Nanotweezer	k_x (pN/(nm.W))	k_y (pN/(nm.W))	k_z (pN/(nm.W))
Ag CDHN	29.4	20.5	227.35
Ag DHN	14.68	39.5	119.37

Spectrum of $|F_z|$ for different values of Φ_{ps} on optimized Ag CDHN nanotweezer is presented at Fig. 6(d). For increasing Φ_{ps}, λ_d red-shifted and $|F_d|$ increased. Effects of λ_d for changing Φ_{ps} was monitored as can be seen in Fig. 6(e). λ_d can be expressed using following equation with respect to Φ_{ps},

$$\lambda_d = 0.5\Phi_{ps} + 1329. \tag{3}$$

Fig. 6(f)–(h) display force and potential components at corresponding λ_d for $\Phi_{ps} =$ 30, 50 and 100 nm. Stable trapping can be achieved for all the above cases. Increasing the diameter of the bead exerted higher trapping force and deeper potential well. Therefore, larger beads will require low intensity beam to trap. Similar minor drop in F_x compared to F_y was observed in these cases.

In Table II, the parameters of the proposed design are compared to those of previous theoretical studies using MST method that trapped PS beads with diameters near 30 nm. According to a recent report, Si dimer with ring geometry provided better thermal performance but lacked in trapping performance, as evidenced by the threshold intensity requirement [15]. A similar performance trait was observed with slotted photonic crystal cavity and slot waveguide based optical nanotweezer designs [46], [47]. On the other hand, Au nanostructures on glass substrates or on Si waveguides demonstrated enhanced trapping stiffness and reduced source power requirement [16], [48]–[50]. An analysis on Ag coaxial plasmonic aperture revealed a trapping stiffness of 1.05 pN/(nm.W) on a 10 nm sized PS bead with source beam power requirement of less than 7 mW [51]. In comparison to these reports, the proposed Ag CDHN design requires several times less threshold power and had better trapping stiffness when trapping a PS bead with a diameter of 30 nm. Ag CDHN also focuses on improving heat sink capability, which was missing from the other reports. A heat sink capable nanotweezer using Au DHN nanostructure demonstrated a 0.64 mW threshold power requirement for trapping a 100 nm sized bead [33]. Our proposed CDHN design is more efficient than the previous report due to it's improved geometry increased field intensity at the center. As a result, the beam power requirement is reduced by 45% while trapping a 100 nm sized bead.

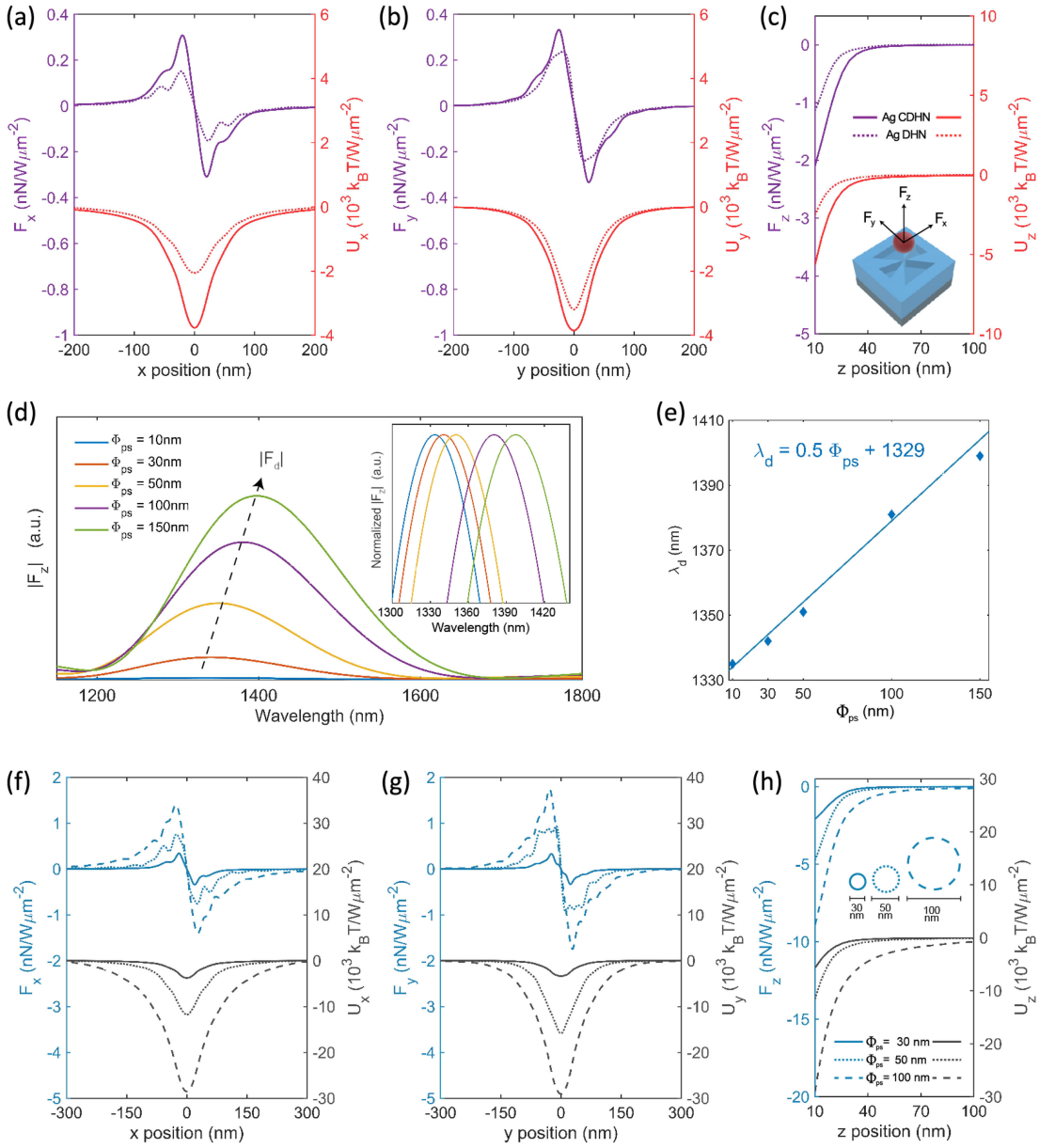

Fig. 6. Trapping force and potential for Ag CDHN (solid line) and Ag DHN (dotted line) nanotweezers with 30 nm PS sphere moving along (a) x axis (F_x, U_x), (b) y axis (F_y, U_y) and (c) z axis (F_z, U_z). (d) Wavelength spectrum of $|F_z|$ at the central location of Ag CDHN nanotweezer for PS bead diameter, $\Phi_{ps} = 10$, 30, 50, 100, and 150 nm. Inset shows normalized $|F_z|$ for better visualization of shifting of λ_d. (e) Variation of λ_d with respect to Φ_{ps}. (f-h) Trapping force and potential for Ag CDHN with $\Phi_{ps} = 30$ (solid line), 50 (dotted line), and 100 nm (dashed line) at λ_d equalling 1340, 1350, and 1380 nm, respectively.

TABLE II
PERFORMANCE COMPARISON WITH REPORTED GENERATORS

Geometry	n_{ps}	Bead diameter (nm)	Wavelength (nm)	Threshold power (mW)	Threshold intensity ($mW/\mu m^2$)	Maximum horizontal Stiffness	Ref
Si dimer with ring	1.6	20	1064	-	9.5	0.1 fN/nm	[15]
Slotted photonic crystal cavity	1.45	30	1400	10	-	3.49 pN/(nm.W)	[46]
Slot waveguide	1.55	35	1550	8.19	-	0.118 pN/(nm.W)	[47]
Waveguide coupled Au bowtie	1.59	20	1620	10.2	-	-	[16]
Au dual nanohole	1.6	25	1064	-	6.67	0.26 fN/nm	[48]
Au nanohole	1.575	50	1064	-	1.6	6.6 fN/nm	[49]
Modified Au nanohole	-	30	980	-	55	0.48 fN/nm	[50]
Ag coaxial plasmonic aperture	2	10	818	<7	-	1.05 pN/(nm.W)	[51]
Au DHN	1.59	100	1154	0.64	-	-	[33]
Ag CDHN	1.57	30 50 100	1340 1350 1380	1.7 0.54 0.22	2.66 0.85 0.35	29.4 pN/(nm.W) 91.67 pN/(nm.W) 116.82 pN/(nm.W)	This work

V. Conclusion

We proposed a nanotweezer consisting of an Ag cross diabolo aperture structure on a bottom Ag metal film. Superior reflectivity of Ag enhanced the screening effect which resulted in amplified field enhancement at the upper surface of the metal. The resultant effect of four hot spots can be far more impacting than mono diabolo type nanostructures. We comprehensively studied the dependence of structural parameters on trapping wavelength and trapping forces. Charge density at the top and bottom edges of Ag, SPPs, screening, and lightning rod effect impacted trapping properties for variation of Ag thin film height and structural hollow height. Charge density, consequent LSPR coupling at the central edges, and the top sidewalls affected trapping characteristics when hollow bow angles and wing lengths were varied. Theoretical analysis shows that the optimized Ag CDHN nanotweezer can trap a 30 nm diameter PS bead for minimum incident beam intensity of 2.66 $\mathrm{mW}/\mu\mathrm{m}^2$ while generating 2.14 nN/(W.$\mu\mathrm{m}^{-2}$) inward force. Maximum horizontal trapping stiffness of 29.4 pN/(nm.W) was found for our tweezer which is few-order larger than previous studies. Further analyses showed low-powered light source is required for larger beads. Shifting of resonance wavelength due to bead size can be beneficial for nanoparticle sensing applications. Additionally, the proposed nanostructure offers superior heat sink capability similar to previously reported bottom metal film-based nanostructures. This work opens up opportunities for the study of further research on diabolo aperture or notch-based nanotweezers. We believe our optimized CDHN nanotweezer can be a useful tool for the fabrication of nanomaterials, manipulating and assembly of nanoparticles and bioparticles, analyzing the interaction between nanoparticles, and sensing and characterization of nanoparticles.

Acknowledgment

The authors would like to thank and acknowledge the support and facilities received from the Department of EEE, Bangladesh University of Engineering and Technology (BUET).

References

[1] T. D. Bouloumis, D. G. Kotsifaki, X. Han, S. N. Chormaic, and V. G. Truong, "Fast and efficient nanoparticle trapping using plasmonic connected nanoring apertures," *Nanotechnol.*, vol. 32, no. 2, Oct. 2020, Art. no. 0 25507.

[2] P. Purohit, A. Samadi, P. M. Bendix, J. J. Laserna, and L. B. Oddershede, "Optical trapping reveals differences in dielectric and optical properties of copper nanoparticles compared to their oxides and ferrites," *Sci. Rep.*, vol. 10, no. 1, Jan. 2020, Art. no. 1198.

[3] A. Samadi, P. M. Bendix, and L. B. Oddershede, "Optical manipulation of individual strongly absorbing platinum nanoparticles," *Nanoscale*, vol. 9, pp. 18 449–18 455, 2017.

[4] P. J. Pauzauskie, A. Radenovic, E. Trepagnier, H. Shroff, P. Yang, and J. Liphardt, "Optical trapping and integration of semiconductor nanowire assemblies in water," *Nature Mater.*, vol. 5, no. 2, pp. 97–101, Feb. 2006.

[5] B. J. Roxworthy *et al.*, "Application of plasmonic bowtie nanoantenna arrays for optical trapping, stacking, and sorting," *Nano Lett.*, vol. 12, no. 2, pp. 796–801, Feb. 2012.

[6] A. Ashkin and J. M. Dziedzic, "Internal cell manipulation using infrared laser traps," in *Proc. Nat. Acad. Sci.* USA, 1989, pp. 7914–7918.

[7] M.-C. Zhong, X.-B. Wei, J.-H. Zhou, Z.-Q. Wang, and Y.-M. Li, "Trapping red blood cells in living animals using optical tweezers," *Nature Commun.*, vol. 4, no. 1, Apr. 2013, Art. no. 1768.

[8] X. Wang *et al.*, "Enhanced cell sorting and manipulation with combined optical tweezer and microfluidic chip technologies," *Lab Chip*, vol. 11, pp. 3656–3662, 2011.

[9] N. Gupta and A. Dhawan, "Bridged-bowtie and cross bridged-bowtie nanohole arrays as SERS substrates with hotspot tunability and multi-wavelength SERS response," *Opt. Exp.*, vol. 26, no. 14, pp. 17 899–17 915, Jul. 2018.

[10] J. Berthelot, S. S. Aćimović, M. L. Juan, M. P. Kreuzer, J. Renger, and R. Quidant, "Three-dimensional manipulation with scanning near-field optical nanotweezers," *Nature Nanotechnol.*, vol. 9, no. 4, pp. 295–299, Apr. 2014.

[11] M. Urbieta *et al.*, "Atomic-scale lightning rod effect in plasmonic picocavities: A classical view to a quantum effect," *ACS Nano*, vol. 12, no. 1, pp. 585–595, Jan. 2018.

[12] D. Verschueren, X. Shi, and C. Dekker, "Nano-optical tweezing of single proteins in plasmonic nanopores," *Small Methods*, vol. 3, no. 5, 2019, Art. no. 1800465.

[13] Z.-S. Li, T.-W. Lu, P.-R. Huang, and P.-T. Lee, "Efficient nano-tweezers via a silver plasmonic bowtie notch with curved grooves," *Photon. Res.*, vol. 9, no. 3, pp. 281–288, Mar. 2021.

[14] F. Alpeggiani, S. D'Agostino, D. Sanvitto, and D. Gerace, "Visible quantum plasmonics from metallic nanodimers," *Sci. Rep.*, vol. 6, no. 1, Oct. 2016, Art. no. 34772.

[15] Z. Xu, W. Song, and K. B. Crozier, "Optical trapping of nanoparticles using all-silicon nanoantennas," *ACS Photon.*, vol. 5, no. 12, pp. 4993–5001, Dec. 2018.

[16] P.-T. Lin, H.-Y. Chu, T.-W. Lu, and P.-T. Lee, "Trapping particles using waveguide-coupled gold bowtie plasmonic tweezers," *Lab Chip*, vol. 14, pp. 4647–4652, 2014.

[17] C.-H. Lee *et al.*, "Boosted photocatalytic efficiency through plasmonic field confinement with bowtie and diabolo nanostructures under LED irradiation," *Opt. Exp.*, vol. 24, no. 16, pp. 17 541–17 552, Aug. 2016.

[18] B. Grześkiewicz, K. Ptaszyński, and M. Kotkowiak, "Near and far-field properties of nanoprisms with rounded edges," *Plasmonics*, vol. 9, no. 3, pp. 607–614, Jun. 2014.

[19] G. Baffou *et al.*, "Photoinduced heating of nanoparticle arrays," *ACS Nano*, vol. 7, no. 8, pp. 6478–6488, Aug. 2013.

[20] Y. Gao and Y. Shi, "Design of a single nanoparticle trapping device based on bow-tie-shaped photonic crystal nanobeam cavities," *IEEE Photon. J.*, vol. 11, no. 3, pp. 1–8, Jun. 2019.

[21] R. M. Bakker *et al.*, "Magnetic and electric hotspots with silicon nanodimers," *Nano Lett.*, vol. 15, no. 3, pp. 2137–2142, Mar. 2015.

[22] M. Caldarola *et al.*, "Non-plasmonic nanoantennas for surface enhanced spectroscopies with ultra-low heat conversion," *Nature Commun.*, vol. 6, no. 1, Aug. 2015, Art. no. 7915.

[23] S. Komoto *et al.*, "Optical trapping of polystyrene nanoparticles on black silicon: Implications for trapping and studying bacteria and viruses," *ACS Appl. Nano Mater.*, vol. 3, no. 10, pp. 9831–9841, Oct. 2020.

[24] Z. Zhang *et al.*, "Black silicon with order-disordered structures for enhanced light trapping and photothermic conversion," *Nano Energy*, vol. 65, 2019, Art. no. 103992.

[25] N. Descharmes, U. P. Dharanipathy, Z. Diao, M. Tonin, and R. Houdré, "Observation of backaction and self-induced trapping in a planar hollow photonic crystal cavity," *Phys. Rev. Lett.*, vol. 110, Mar. 2013, Art. no. 123601.

[26] K. Wang, E. Schonbrun, P. Steinvurzel, and K. B. Crozier, "Trapping and rotating nanoparticles using a plasmonic nano-tweezer with an integrated heat sink," *Nature Commun.*, vol. 2, no. 1, Sep. 2011, Art. no. 469.

[27] K. Mokri and M. H. Mozaffari, "Numerical design of a plasmonic nanotweezer for realizing high optical gradient force," *Opt. Laser Technol.*, vol. 119, Nov. 2019, Art. no. 105620.

[28] M. Samadi, S. Vasini, S. Darbari, A. A. Khorshad, S. N. S. Reihani, and M. K. Moravvej-Farshi, "Hexagonal arrays of gold triangles as plasmonic tweezers," *Opt. Exp.*, vol. 27, no. 10, pp. 14 754–14 766, May 2019.

[29] I.-C. Huang, J. Holzgrafe, R. A. Jensen, J. T. Choy, M. G. Bawendi, and M. Lončar, "10 nm gap bowtie plasmonic apertures fabricated by modified lift-off process," *Appl. Phys. Lett.*, vol. 109, no. 13, Sep. 2016, Art. no. 133105.

[30] L.-W. Nien, B.-K. Chao, J.-H. Li, and C.-H. Hsueh, "Optimized sensitivity and electric field enhancement by controlling localized surface plasmon resonances for bowtie nanoring nanoantenna arrays," *Plasmonics*, vol. 10, no. 3, pp. 553–561, Jun. 2015.

[31] J. Park, H. Lee, A. Gliserin, K. Kim, and S. Kim, "Spectral shifting in extraordinary optical transmission by polarization-dependent surface plasmon coupling," *Plasmonics*, vol. 15, no. 2, pp. 489–494, Nov. 2019.

[32] M. Hrtoň, A. Konečná, M. Horák, T. Šikola, and V. Křápek, "Plasmonic antennas with electric, magnetic, and electromagnetic hot spots based on babinet's principle," *Phys. Rev. Appl.*, vol. 13, no. 5, May 2020, Art. no. 054045.

[33] Y.-C. Lin and P.-T. Lee, "Efficient optical trapping and detection of nanoparticle via plasmonic bowtie notch," *IEEE Photon. J.*, vol. 11, no. 2, pp. 1–10, Apr. 2019.

[34] M. A. Hasan and A. Zubair, "Efficient silver diabolo hollow notch plasmonic nanotweezer with improved heat sink capability," *Proc. IEEE Int. Conf. Telecommun. Photon. (ICTP)* Dec. 2021, pp. 1–4.

[35] P. B. Johnson and R. W. Christy, "Optical constants of the noble metals," *Phys. Rev. B*, vol. 6, pp. 4370–4379, Dec. 1972.

[36] E. D. Palik, *Handbook of Optical Constants of Solids*, 1st ed. Orlando, FL, USA: Academic Press, 1985.

[37] J. F. Shackelford, Y.-H. Han, S. Kim, and S.-H. Kwon, *CRC Materials Science and Engineering Handbook*. Boca Raton, FL, USA: CRC Press, Apr. 2016.

[38] T. V. Raziman, R. J. Wolke, and O. J. F. Martin, "Optical forces in nanoplasmonic systems: How do they work, what can they be useful for," *Faraday Discuss.*, vol. 178, pp. 421–434, 2015.

[39] R. A. Jensen *et al.*, "Optical trapping and two-photon excitation of colloidal quantum dots using bowtie apertures," *ACS Photon.*, vol. 3, no. 3, pp. 423–427, Mar. 2016.

[40] L. Wu, P. Bai, and E. P. Li, "Designing surface plasmon resonance of subwavelength hole arrays by studying absorption," *J. Opt. Soc. Am. B*, vol. 29, no. 4, pp. 521–528, Apr. 2012.

[41] K. L. Göeken, V. Subramaniam, and R. Gill, "Enhancing spectral shifts of plasmon-coupled noble metal nanoparticles for sensing applications," *Phys. Chem. Chem. Phys.*, vol. 17, pp. 422–427, 2015.

[42] T. Kaseberg, T. Siefke, S. Kroker, and B. Bodermann, "Inverted plasmonic lens design for nanometrology applications," *Meas. Sci. Technol.*, vol. 31, no. 7, pp. 74013–74023, 2020.

[43] A. Degiron, H. J. Lezec, W. L. Barnes, and T. W. Ebbesen, "Effects of hole depth on enhanced light transmission through subwavelength hole arrays," *Appl. Phys. Lett.*, vol. 81, no. 23, pp. 4327–4329, 2002.

[44] W. Ding, R. Bachelot, S. Kostcheev, P. Royer, and R. E. D. Lamaestre, "Surface plasmon resonances in silver bowtie nanoantennas with varied bow angles," *J. Appl. Phys.*, vol. 108, no. 12, 2010, Art. no. 124314.

[45] A. E. Cetin, "FDTD analysis of optical forces on bowtie antennas for high-precision trapping of nanostructures," *Int. Nano Lett.*, vol. 5, no. 1, pp. 21–27, Mar. 2015.

[46] L. Wang, Y. Cao, T. Zhu, R. Feng, F. Sun, and W. Ding, "Optical trapping of nanoparticles with tunable inter-distance using a multimode slot cavity," *Opt. Exp.*, vol. 25, no. 24, pp. 29 761–29 768, Nov. 2017.

[47] A. H. J. Yang, T. Lerdsuchatawanich, and D. Erickson, "Forces and transport velocities for a particle in a slot waveguide," *Nano Lett.*, vol. 9, no. 3, pp. 1182–1188, Mar. 2009.

[48] Z. Xu, W. Song, and K. B. Crozier, "Direct particle tracking observation and brownian dynamics simulations of a single nanoparticle optically trapped by a plasmonic nanoaperture," *ACS Photon.*, vol. 5, no. 7, pp. 2850–2859, Jul. 2018.

[49] M. L. Juan, R. Gordon, Y. Pang, F. Eftekhari, and R. Quidant, "Self-induced back-action optical trapping of dielectric nanoparticles," *Nature Phys.*, vol. 5, no. 12, pp. 915–919, Dec. 2009.

[50] X. Han, V. G. Truong, P. S. Thomas, and S. N. Chormaic, "Sequential trapping of single nanoparticles using a gold plasmonic nanohole array," *Photon. Res.*, vol. 6, no. 10, pp. 981–986, Oct. 2018.

[51] A. A. E. Saleh and J. A. Dionne, "Toward efficient optical trapping of sub-10-nm particles with coaxial plasmonic apertures," *Nano Lett.*, vol. 12, no. 11, pp. 5581–5586, Nov. 2012.